Stagnation of Flow in Protein Cavities by Boundary Element Microhydrodynamics[†]

Sergio R. Aragon* and David K. Hahn

Department of Chemistry and Biochemistry, San Francisco State University, San Francisco, California

Received: August 29, 2008; Revised Manuscript Received: November 3, 2008

In this work, we apply the boundary element method to describe the fluid velocity profiles in pockets in protein surfaces that are crucial to their function as enzymes. First, we study a simplified model, that of a dimpled sphere, in order to properly interpret the behavior in more complex surfaces such as proteins. In that case, we are able to observe the difference between an unphysical sharp edge for the dimple and a smooth edge. The sharp edge produces extra dissipation in the fluid, accounting for much more friction for all types of body motions. We were able to observe the direct correlation of the stagnation depth with the depth of the dimple in this simple case, allowing us to interpret this feature in a similar fashion for proteins. We have found that the fluid in the protein pockets translates with the body, irrespective of the direction body motion, for a distance comparable to the size of the pocket, and that such stagnation volumes are larger for motions parallel to the pocket axis. Outside of these pockets, the fluid velocity profile decays to that of the surrounding fluid far away from the protein (taken to be zero in our case, for convenience), as the Oseen tensor requires. We have also found that there is weak local motion of fluid inside of the pockets, with velocities about 1% of those of the body. This study suggests that there may be a role for the hydrodynamics of solvent inside of pockets for the transport of substrates to protein active sites. If solvent is effectively stagnant inside of a pocket, then transport must occur by diffusion near the pocket surface even if the fluid around the protein is stirred. The weak local motions inside of the pocket may also be relevant in this transport process, but these may be easily overwhelmed by any electrostatic interactions that are likely present at active sites.

I. Introduction

In a previous work,[1] we have reported on the development of a very precise boundary element method (BE) and a program suite (BEST) for the computation of transport tensors of macromolecules under the stick boundary condition. BEST was thereafter applied to the computation of transport properties[2,3] of proteins including translational diffusion, the rotational diffusion tensor, and the intrinsic viscosity. Our very accurate and precise hydrodynamic model enabled us to compute transport properties in excellent agreement with experiment, except for a few notorious cases. In these very small proteins with flexible chains or some multimeric proteins, we were able to argue that the crystal structure does not represent the actual solution structure. These findings are being corroborated by extensive molecular dynamics simulations that will be reported elsewhere. In this paper, we report on the use of BEST for the investigation of the hydrodynamic trapping of solvent in pockets in soluble protein surfaces that are crucial to their function as enzymes.

The boundary element method allows the computation of transport properties with unprecedented accuracy because it depends on an exact formulation of the Stokes flow equations[4−6] and does not depend at all on approximate hydrodynamic interaction tensors commonly used in bead representations of molecules.[7] In addition to this laboratory, several other authors have used the boundary element method to compute diffusion coefficients with stick[8] or slip boundary conditions,[9,10] intrinsic viscosity,[9] and electrophoretic mobilities[11−14] with great success. In particular, Allison[14] has previously used the boundary element method to describe the velocity field away from the surface of a biomolecule. Thus, the boundary element method is well established and a method of choice for accurate and precise computations. In the next section, we briefly review the basic equations of this method.

II. Theory: The Boundary Element Method for Stick Boundary Conditions

For macromolecules, consideration of the solvent as a continuum is an excellent approximation, and the governing equations for the computation of the hydrodynamic transport properties are the Navier−Stokes equations of fluid flow. In the limit of a small Reynolds number, as appropriate for the diffusion process, the equations are known as the Stokes or creeping flow equations.[4] Whereas bead methods aim to solve a mobility problem, which cannot be formulated exactly, an alternative method is to solve a resistance problem, which can be formulated exactly. As is shown below, once one has precise friction tensors, it is straightforward to compute the diffusion tensors. In the mid 1970s, Youngren & Acrivos[5] presented an effective method for the numerical solution to the exact surface integral representation of the velocity field for the creeping flow equations.

For the case of macromolecules, "stick" boundary conditions are appropriate. In this case, the velocity field of the flow, $\mathbf{v}(\mathbf{y})$ at position $\mathbf{y}$ in the fluid, can be written as an integral over the particle surface (SP)

$$\mathbf{v}(\mathbf{y}) = \mathbf{u_o}(\mathbf{y}) + \int_{sp} \vec{\mathbf{T}}(\mathbf{x},\mathbf{y})\cdot\mathbf{f}(\mathbf{x})\mathrm{d}S_x \qquad (1)$$

where $\mathbf{u_o}(\mathbf{y})$ is the flow velocity of the fluid if the particle was not there (which can be taken to be zero for diffusive motion)

[†] Part of the "J. Michael Schurr Special Section".

* aragons@sfsu.edu.

10.1021/jp807706q CCC: $40.75
Published on Web 12/22/2008

and $\overleftrightarrow{\mathbf{T}}(\mathbf{x},\mathbf{y})$ is the Oseen hydrodynamic interaction tensor. The surface stress force, $\mathbf{f}(\mathbf{x})$ is the unknown quantity that we must obtain. Once this quantity is known, not only can the transport properties of the macromolecule can be directly computed but also the velocity field for any point $\mathbf{y}$ outside of the body. The computation of the velocity field outside of the body is then a two-step process. First, we take the point $\mathbf{y}$ on the surface and move the body with a known velocity field to obtain the unknown surface stress forces on the surface of the body; second, we can then use eq 1 to compute the velocity field at any other point $\mathbf{y}$ in the fluid for that body motion.

The Oseen tensor is given by[4,15]

$$\overleftrightarrow{\mathbf{T}}(\mathbf{x},\mathbf{y}) = \frac{1}{8\pi\eta|\mathbf{x}-\mathbf{y}|}\left[\overleftrightarrow{\mathbf{I}} + \frac{(\mathbf{x}-\mathbf{y})(\mathbf{x}-\mathbf{y})}{|\mathbf{x}-\mathbf{y}|^2}\right] \quad (2)$$

Since eq 1 is an integral equation, the solution requires an approximate numerical method. The method, however, can be iterated to obtain arbitrary precision. The first step is to discretize the surface by replacing it with a collection of N patches that smoothly tile the molecular surface and to consider the velocity field for points $\mathbf{y}$ on the surface of the arbitrarily shaped body. We can then write

$$\mathrm{SP} = \sum_{j=1}^{N} \Delta_j \quad (3)$$

We place the coordinate $\mathbf{x}_j$ at the center of the small patch Δ_j and take the surface stress force $\mathbf{f}(\mathbf{x})$ to be a constant over the entire patch area. This is the basic approximation; it is clear that it will become a better and better approximation as the patch is made small. Thus, an extrapolation to zero size patch leads to a very precise value for the transport properties and the unknown surface stress forces. With this approximation, eq 1 becomes a set of $3N$ equations for the $3N$ unknowns, $\mathbf{f}_j = \mathbf{f}(\mathbf{x}_j)$

$$\mathbf{v}(\mathbf{y}_k) = \sum_{j=1}^{N} \overleftrightarrow{\mathbf{G}}_{kj} \cdot \mathbf{f}_j \quad (4)$$

The centerpiece of this set of equations is a set of N completely known 3×3 matrices of coefficients that contain all geometric information, the integrals of the Oseen tensor over a surface patch

$$\overleftrightarrow{\mathbf{G}}_{kj} = \int_{\Delta_j} \overleftrightarrow{\mathbf{T}}(\mathbf{x},\mathbf{y}_k)\mathrm{d}S_{\mathrm{x}} \quad (5)$$

In addition to the introduction of a robust regularization method, the other significant advance made in our work is the essentially exact integration of the Oseen tensor in the above expression. The set of $3N$ equations can be written all at once

$$\begin{bmatrix} \mathbf{v}_1 \\ .. \\ .. \\ \mathbf{v}_N \end{bmatrix}_{3N\times 1} = \begin{bmatrix} \overleftrightarrow{\mathbf{G}}_{11} & .. & .. & \overleftrightarrow{\mathbf{G}}_{1N} \\ .. & .. & .. & .. \\ .. & .. & .. & .. \\ \overleftrightarrow{\mathbf{G}}_{N1} & .. & .. & \overleftrightarrow{\mathbf{G}}_{NN} \end{bmatrix}_{3N\times 3N} \begin{bmatrix} \mathbf{f}_1 \\ .. \\ .. \\ \mathbf{f}_N \end{bmatrix}_{3N\times 1} \quad (6)$$

from which the unknown surface stress forces can be readily obtained by matrix inversion of the $3N\times 3N$ supermatrix $\overleftrightarrow{\mathbf{G}}$,

$$[\mathbf{f}]_{3N\times 1} = [\overleftrightarrow{\mathbf{G}}]^{-1}_{3N\times 3N}[\mathbf{v}]_{3N\times 1} \quad (7)$$

In previous work,[1] we have described in detail how to use the surface stress forces to compute the total force and torque on the body in order to obtain the friction tensors and subsequently the diffusion tensors. In the present case, with the $\mathbf{f}(\mathbf{x})$ in hand, we additionally wish to return to eq 1 and recompute the Oseen tensor matrices for points $\mathbf{y}$ outside of the body and perform the integral by a discrete summation over the triangular surface patches of the body. In order to study the hydrodynamic stagnation for a variety of motions, we let the body have specific translation velocity $\mathbf{v}_\mathrm{p}$ and angular velocity $\boldsymbol{\omega}_\mathrm{p}$ (for example $\omega_\mathrm{p} = 0$ and $\mathbf{v}_\mathrm{p} = (v_\mathrm{x},0,0)$) to carry out the above sequence of computations. In sections III and IV below, we study six different motions, three translations and three rotations, in order to determine the velocity fields in dimpled spheres and pockets of various proteins. The points $\mathbf{y}$ outside of the body are chosen along a vector emanating from one of the surface triangles, and the velocity field is computed as a function of that distance.

III. Dimpled Sphere

In order to understand the phenomenon of flow stagnation or hydrodynamic trapping, we first study the behavior in a very simple model, a dimpled sphere. In this case, we make a cavity in a sphere in various ways and determine the velocity field as a function of distance from the center of the cavity and other interesting positions. In Figure 1, we have a sphere that has been dimpled to varying degrees with the depth of the dimple from largest to smallest in A−D. Note that the edge of the dimple is sharp in this model. The radius of the dimple has been arbitrarily chosen to about 1/3 the radius of the sphere, $a = 1$ Å.

The hydrodynamic transport tensors have been determined as presented in previous work[1−3] and are shown in Table 1. For convenience, the two components of the symmetric diffusion tensors are given in internal BEST units where a factor of $kT/8\pi\eta a$ has been factored out. In these units, this unit radius sphere has an exact rotational diffusion coefficient of 1 Å^{-3} and an exact translational diffusion coefficient of 4/3 Å^{-1}. It is noteworthy that the diffusion coefficients in Table 1 differ from those of a perfect sphere by only a few percent. We will see below that the effect of the missing portion of the sphere is compensated to a large degree by the sharpness of the edge in the model. The transport tensor values in Table 1 correspond to an extrapolation to an infinite number of triangles; therefore, the edge sharpness has been properly taken into account. Note also the smallness of the effect of the depth of the dimple in this case.

The data in Table 1 (and that in Table 2 below) have a simple rationalization. We note that all of the values of the components of the diffusion tensors are larger than those of the perfect sphere, which has 1.33333 for Dt and 1.0000 Dr. This result follows in a straightforward way from general extremum principles derived originally by Hill And Power.[16] Their extremum principle implies that the hydrodynamic drag or friction for any object whose surface totally encompases that of another object is larger for both translation and rotational motions. In our case, the perfect sphere is an object that totally encompases a dimpled sphere, whether with sharp or smooth edges as considered below. The extremum principle implies that the friction should be largest for the perfect sphere, and since the diffusion coefficients are inversely related to the friction, the dimpled spheres should have the larger diffusion tensor

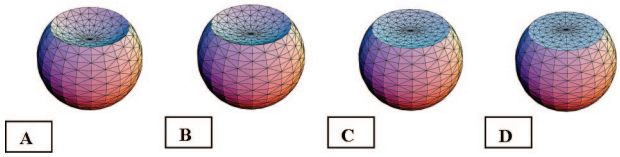

Figure 1. Dimpled spheres; (A) deep dimple to (D) flat dimple.

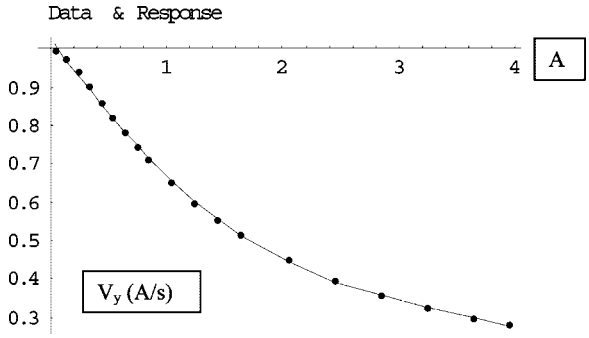

Figure 2. Fluid velocity normal to the surface as a function of distance from a triangle on the side of the sphere. The sphere is translating in the y direction with a speed of 1 Å/s.

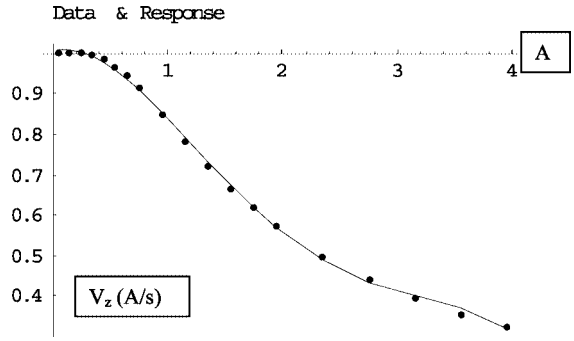

Figure 3. Fluid velocity normal to the surface as a function of distance from a triangle at the center of the simple sphere. The sphere is translating in the z direction with a speed of 1 Å/s.

TABLE 1: Dimpled Sphere Hydrodynamic Data

surface	$Dt_{\perp}$	$Dt_{\parallel}$	$Dr_{\perp}$	$Dr_{\parallel}$
A	1.3647	1.3368	1.0584	1.0146
B	1.3641	1.3367	1.0579	1.0141
C	1.3617	1.3361	1.0556	1.0124
D	1.3602	1.3359	1.0517	1.0110

TABLE 2: Transport Tensors for Smooth Dimpled Spheres and a Sphere

surface	area	$Dt_{\perp}$	$Dt_{\parallel}$	$Dr_{\perp}$	$Dr_{\parallel}$
A	11.935	1.4131	1.3503	1.1488	1.0536
B	12.209	1.3681	1.3390	1.0689	1.0163
C	12.566	1.3333	1.3334	1.0001	0.9998

components. In addition, sphere D with a flat dimple has a surface that encompases all other spheres; thus, the values for this sphere should be the smallest in the set. Our computations are in perfect agreement with the general extremum principles.

In Figures 2 and 3, we show the velocity profile for the large component of the velocity as a function of distance from the face of a chosen triangle in dimpled sphere A. In Figure 2, the triangle is outside of the dimple, on the side of the sphere. The basic observable feature is the expected $1/R$ decay of the velocity, starting with the value of 1 Å/s at the surface. There is no evidence of water traveling with the same speed as the sphere at distances larger than 0.1 Å; the decay starts immediately as the distance from the surface increases.

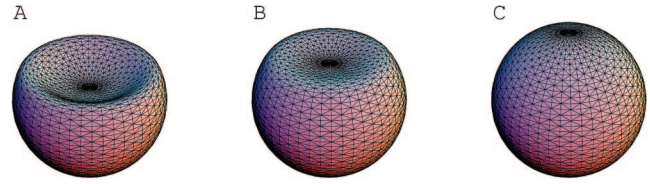

Figure 4. Dimpled spheres with a smooth edge: A and B. C is a perfect sphere with a polar tessellation.

On the other hand, in Figure 3, the velocity profile is shown as a function of distance from the center of a triangle at the bottom of the dimple. In this case, we see something quite different; in addition to the normal decay with distances at values larger than 1 Å, close to the sphere surface, inside of the dimple, the velocity profile does not decay at all, indicating that this parcel of solvent is traveling along with the sphere. The solvent in this case has been caught in the dimple and is stagnant with respect to the surface. The stagnation region extends to about 0.5 Å, comparable to the depth of the dimple.

In order to determine the effect of the sharp edge, we also studied a dimple with rounded edges as seen in Figure 4. The transport tensors are shown in Table 2.

It is immediately obvious, by comparison with Table 1, that the smooth dimpled spheres differ from a perfect sphere much more than those dimpled spheres with a sharp-edged dimple. The dimpled sphere labeled "A" has the same size and depth of dimple for the cases of the sharp-edged and the smooth-edge dimples. The transport tensor components are significantly larger than those of a perfect sphere, indicating that there is less friction with the solvent in the case of the smooth dimples. For example, the perpendicular translational diffusion and rotational diffusion coefficients differ from a perfect sphere by 6 and 15%, respectively, in the case of the smooth dimpled sphere A, whereas in the equivalent sharp-edged dimpled sphere, the differences are only 2.4 and 5.8%, respectively. The sharp edge of the dimple does introduce considerable friction. Note that the data for the perfect sphere show that the computations are accurate to 0.01%—nearly numerically exact.

The extremum principles of Hill and Power can also be applied to understand the relationship between the sharp-edged and smooth-edged spheres. The dimpled sphere A with a sharp edge of Table 1 was smoothed to produce the smooth-edge dimpled sphere of Table 2. In this case, the sharp-edged sphere totally encompases the smooth-edged sphere. The extremum principle implies that the friction of the smooth sphere has to be less for any of its motions, and the diffusion coefficients should thereby be larger. This is exactly the case as shown in the tabulated data.

In Figure 5, we show the velocity profiles as a function of distance from the center of a triangle as before.

For the perfect sphere "C", Figure 5 shows that the decay starts immediately, while for the dimpled spheres, the decay is delayed for a larger distance as the dimple depth increases. In addition, Figure 5 shows that the fluid stagnation is larger when the sphere is moved along the axis of the dimple compared to a motion perpendicular to it. In other words, the fluid is more effectively trapped in the cavity as the cavity is moved forward, compared to moving the cavity sideways.

One can also ask if there is any interesting motion detected inside of the cavity. We can get an idea of this by observing the smaller transverse components of the fluid velocity inside of the cavity. In Figure 6, we show the x and y components of the fluid velocity vector when the smooth dimpled sphere is translated along the z axis, as a function of distance from the

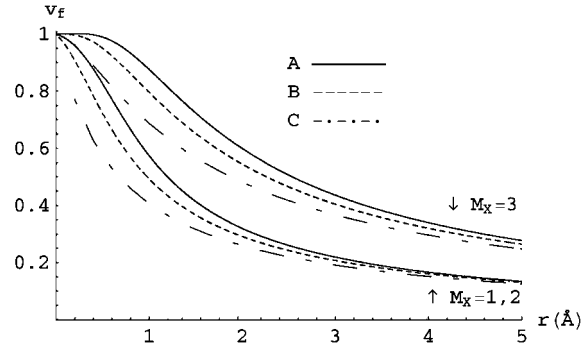

Figure 5. The velocity decay as a function of distance from a surface triangle in the center of the dimple for each of the spheres A, B, and C. The values of M_x indicate translational motion parallel to the dimple axis (3) and perpendicular to the dimple axis (1, 2).

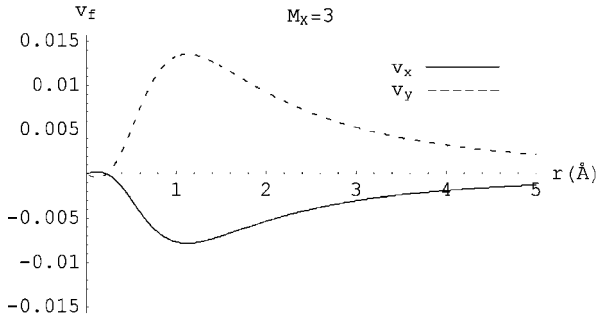

Figure 6. The transverse velocity components decay as a function of distance from a surface triangle in the center of the dimple for the smooth dimpled sphere A. The value of $M_x = 3$ indicates translational motion of the body parallel to the dimple axis (3). Note the opposite sign of the x and y components of the velocity.

dimple center triangle. The transverse velocity components are very small, barely over 1% of the value of the main z component, and they decay to zero as the distance from the dimple increases, as should be the case. The fact that the x and y components differ in sign indicates that there is some type of local circulation inside of the hydrodynamic trapped water in the dimple.

IV. Stagnation of Fluid in Protein Pockets

Proteins often have significant cavities in their surface related to their function, sites for the docking of a substrate in an enzyme, for example. In this section, we study the fluid velocity as we go out of pockets in three different proteins, lysozyme, myoglobin, and albumin. In our previous work,[2,3] we have determined a uniform surface hydration model that properly describes the transport of proteins over a large range of molecular weights. The hydrated surface and the molecular surface are determined by means of the MSROLL program of Connolly,[17−20] with a probe radius of 1.5 Å to represent water. The molecular surface is defined by the Connolly surface obtained from the van der Waals radii of the protein atoms. Since hydrogen is typically not detected, a modified set of radii is used that contains slightly enlarged heteroatoms when these are hydrogen bonded to them. The volume enclosed by the molecular surface is the protein excluded volume, V_0. In order to represent hydration, we add a thickness δ to all radii and perform the Connolly roll once more. The larger surface so obtained is the hydrated surface. The value of δ used is 1.1 Å. For full details of this process, see ref 2.

In our study of proteins, we have selected triangles in three surface locations, on a surface bump of the protein where there is no pocket, inside of a medium pocket, and inside of a deep pocket. In Figures 7−9 below, the vectors emanate from such chosen triangles, and the velocity has been determined for positions along that vector. Furthermore, for each selected vector, the protein has been translated parallel and perpendicular to this vector. This is achieved by applying a rotation matrix to all atomic positions in the crystal structure to orient the protein along the desired direction before the hydrodynamic computations are carried out.

For each of these proteins, the basic features that we observed in the case of the dimpled spheres are present. When the triangle is on a surface bump, where there is no pocket, the velocity profile decays immediately with distance along the chosen vector (the dot−dashed lines in Figures 7−9), and there is no evidence of fluid stagnation. For the deep pockets, the picture is very clear; there is significant stagnation, even more than that observed for the dimpled spheres, for distances comparable to the depth of the pocket (the solid lines in Figures 7−9). The velocity profile does not decay until the distance is larger than the pocket depth. For medium-sized pockets, the profile is intermediate between the previous two (the dotted lines in Figures 7−9). Another feature of the fluid stagnation in the deep pockets is the abruptness of the decay for the motions perpendicular to the vector in the pocket. The depth of stagnation is generally larger for motion along the vector ($M_x = 3$), but the velocity for perpendicular motions ($M_x = 1,2$) decays faster after the stagnation region compared to the leisure decay in the parallel motion.

Albumin, the protein with the deepest pockets, shows the largest amount of fluid stagnation, with only 10% decay over a distance of 30 Å, while myoglobin, with the shallowest pockets, shows such decay over a distance of 15 Å. Lysozyme is intermediate between these two. As with the dimpled spheres, weak local fluid motion inside of the cavities can also be detected. In Figure 10, we show an example for albumin.

The transverse components have opposite signs, as in the case of the dimpled sphere, indicating some type of weak local fluid motion, with amplitudes of about 1% of the total body motion. Many more samples at different points along the pocket would have to be taken to fully describe the fluid motion stream lines. The lack of symmetry in the pocket results in a more irregular velocity component profile compared to the dimpled sphere.

V. Discussion and Conclusions

We have shown that a precise implementation of the boundary element method allows the computation of hydrodynamic transport tensors and velocity profiles outside of a hydrodynamic body to high precision for arbitrarily shaped bodies such as proteins. In this work, we have applied our tools to describe the velocity profiles in pockets in protein surfaces that are crucial to their function as enzymes. We have found that the fluid in the pockets translates with the body, irrespective of the direction body motion, for a distance comparable to the size of the pocket, and that such stagnation volumes are larger for motions parallel to the pocket axis. Outside of these pockets, the fluid velocity profile decays to that of the surrounding fluid far away from the protein (taken to be zero in our case, for convenience), as the Oseen tensor requires. We have also found that there is weak local motion of fluid inside of the pockets, with velocities about 1% of those of the body.

All of these features are also observed in a simplified model, that of a dimpled sphere, which we studied in order

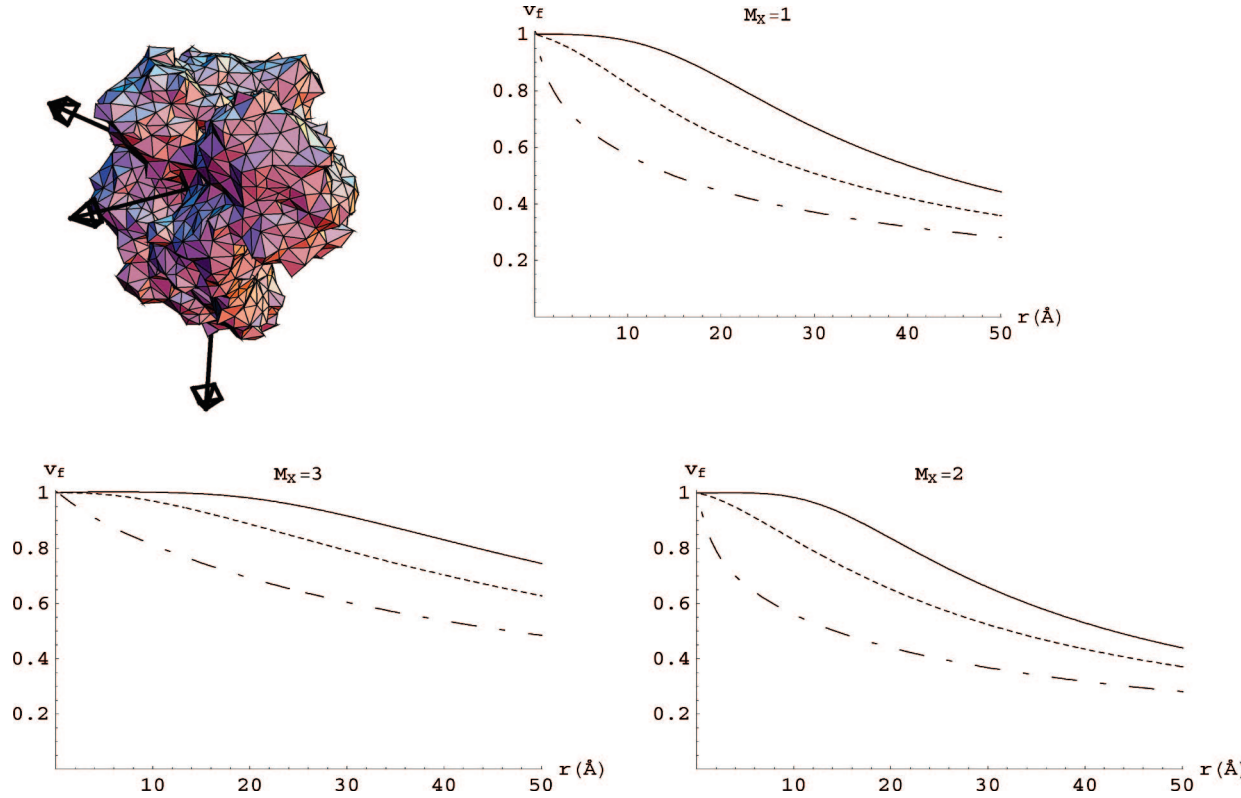

Figure 7. Fluid stagnation in Albumin (1AO6). The solid line represents a deep pocket in the middle of the protein, the dotted line represents a medium pocket at the top left of the protein, while the dashed line represents a triangle at the bottom of the protein, where there is no pocket. $M_x = 3$ represents protein motion parallel to the vector, while $M_x = 1, 2$ constitutes motion perpendicular to the vector.

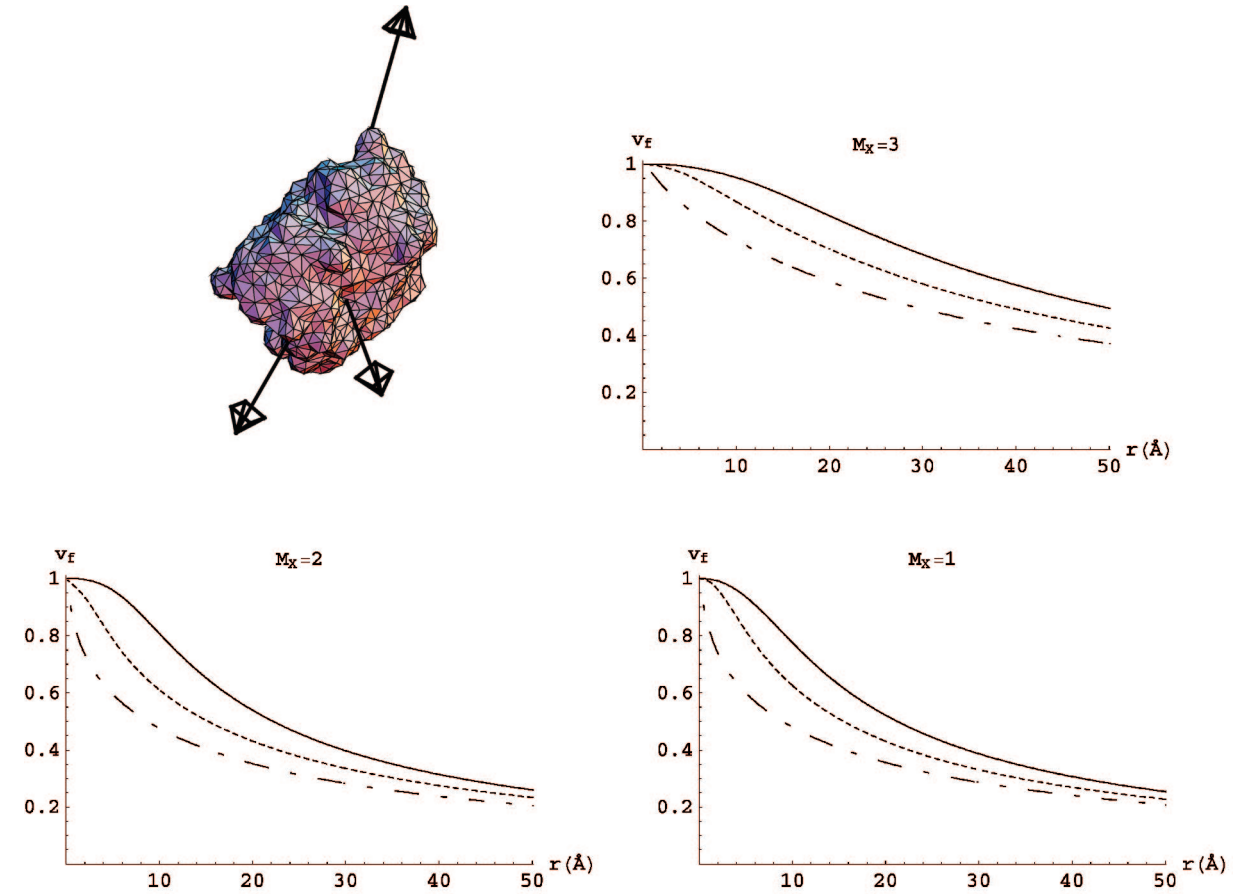

Figure 8. Fluid stagnation in myoglobin (1MBO). The solid line represents a deep pocket in the right-hand side of the protein, the dotted line represents a medium pocket at bottom of the protein, while the dashed line represents a triangle at the top of the protein, where there is no pocket. $M_x = 3$ represents protein motion parallel to the vector, while $M_x = 1, 2$ constitutes motion perpendicular to the vector.

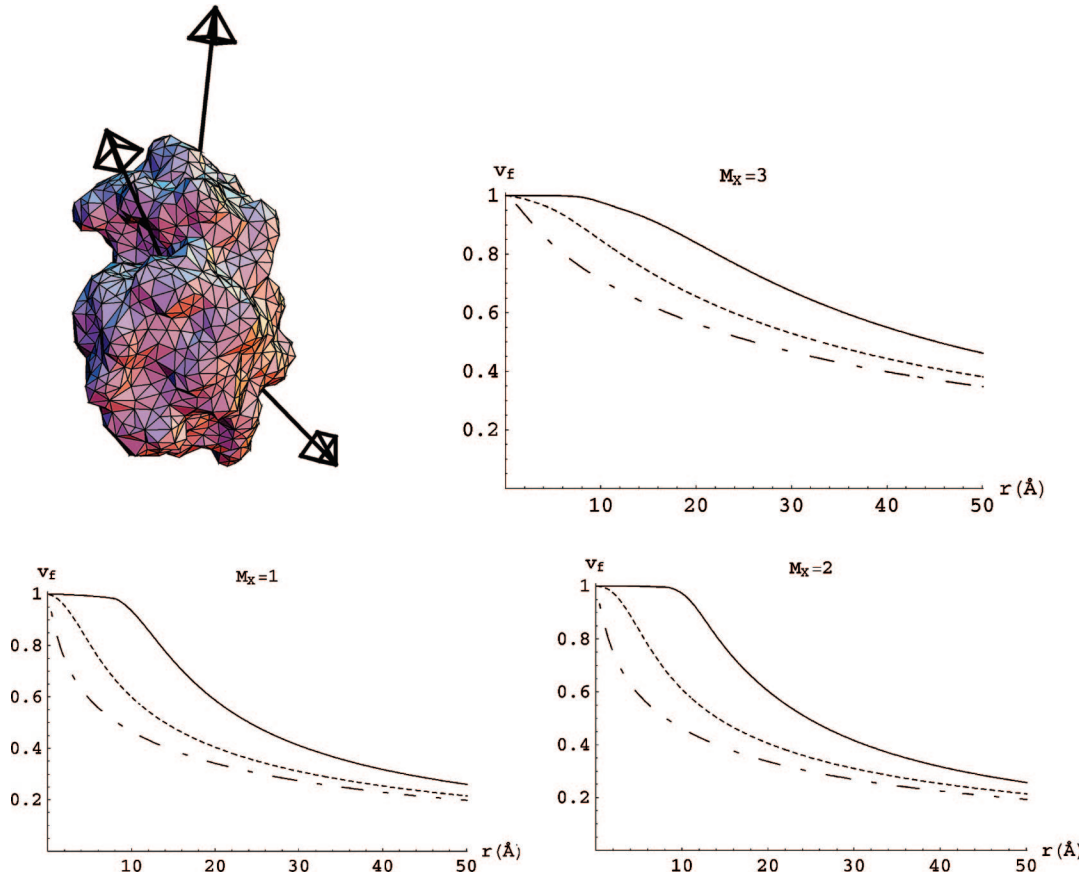

Figure 9. Fluid stagnation in lysozyme (2CDS). The solid line represents a deep pocket in the top left of the protein, the dotted line represents a medium pocket at the bottom right of the protein, while the dashed line represents a triangle at the top of the protein, where there is no pocket. $M_x = 3$ represents protein motion parallel to the vector, while $M_x = 1, 2$ constitutes motion perpendicular to the vector.

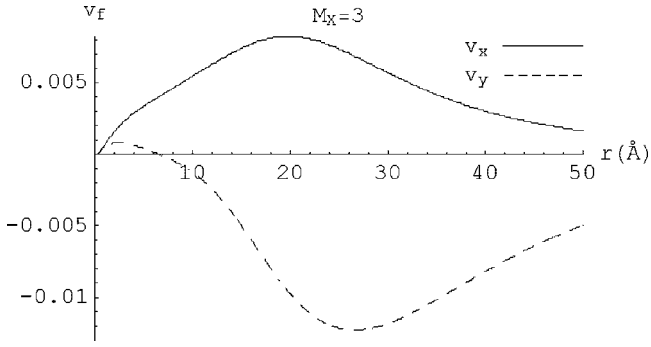

Figure 10. The transverse velocity components decay as a function of distance from a surface triangle in the center of the deep pocket for albumin. The value of $M_x = 3$ indicates translational motion of the body parallel to the pocket vector. Note the opposite sign of the x and y components of the velocity.

to properly interpret the behavior in more complex surfaces such as proteins. In that case, we were also able to observe the difference between an unphysical sharp edge for the dimple and a smooth edge. The sharp edge produces extra dissipation in the fluid, accounting for much more friction for all types of body motions. We were able to observe the direct correlation of the stagnation depth with the depth of the dimple in this simple case, allowing us to interpret this feature in a similar fashion for proteins.

This study suggests that there may be a role for the hydrodynamics of solvent inside of pockets for the transport of substrates to protein active sites. If solvent is effectively stagnant inside of a pocket, then transport must occur by diffusion near the pocket surface even if the fluid around the protein is stirred. The weak local motions inside of the pocket may also be relevant in this transport process, but these may be easily overwhelmed by any electrostatic interactions that are likely present at active sites.

Acknowledgment. This research was supported through a grant from the National Institutes of Health, MBRS SCORE Program, Grant #S06 GM52588.

References and Notes

(1) Aragón, S. R. A precise boundary element method for macromolecular transport properties. *J. Comput. Chem.* **2004**, *25*, 1191–1205.

(2) Aragon, S. R.; Hahn, D. K. Precise boundary element computation of protein transport properties: Diffusion tensors, specific volume, and hydration. *Biophys. J.* **2006**, *91*, 1591–1603.

(3) Hahn, D. K.; Aragon, S. R. The intrinsic viscosity of proteins from high precision boundary element calculations. *J. Chem. Theory Comput.* **2006**, *2*, 12–17.

(4) Kim, S.; Karilla, S. J. *Microhydrodynamics*; Butterworth-Heinemann: New York, 1991.

(5) Youngren, G. K.; Acrivos, A. Stokes flow past a particle of arbitrary shape: a numerical method of solution. *J. Fluid Mech.* **1975**, *69*, 377–402.

(6) Wegener, W. A. On an exact starting expression for macromolecular hydrodynamic models. *Biopolymers* **1986**, *25*, 627–637.

(7) Rotne, J.; Prager, S. Variational treatment of hydrodynamic interaction in polymers. *J. Chem. Phys.* **1969**, *50*, 4831–4837.

(8) Brune, D; Kim, S. Predicting protein diffusion coefficients. *Proc. Natl. Acad. Sci. U.S.A.* **1993**, *90*, 3835–3839.

(9) Allison, S. A. Low Reynolds number transport properties of axisymmetric particles employing stick and slip boundary conditions. *Macromolecules* **1999**, *32*, 5304–5312.

(10) Hu, C. M.; Zwanzig, R. Rotational friction coefficients for spheroids with the slipping boundary condition. *J. Chem. Phys.* **1974**, *60*, 4354–4357.

(11) Allison, S. A.; Nambi, P. Transport of charged macromolecules in an electric field by a numerical method. I. Application to a sphere. *Macromolecules* **1992**, *25*, 3971–3978.

(12) Allison, S. A.; Nambi, P. Electrophoresis of spheres by a discretized integral equation/finite difference approach. *Macromolecules* **1994**, *27*, 1413–1422.

(13) Allison, S. A.; Tran, V. T. Modeling the electrophoresis of rigid polyions—Application to lysozyme. *Biophys. J.* **1995**, *68*, 2261–2270.

(14) Allison, S. A.; Mazur, S. Modeling the free solution electrophoretic mobility of short DNA fragments. *Biopolymers* **1998**, *46*, 359–373.

(15) Oseen, C. W. *Hydrodynamik*; Academiches Verlag: Leipzig, 1927.

(16) Hill, R.; Power, G. Extremum principles for slow viscous flow and the approximate calculation of drag. *Q. J. Mech. Appl. Math.* **1956**, *9*, 313–319.

(17) Connolly, M. L. Molecular surface program. *QCPE Bull.* **1981**, *1*, 75–83.

(18) Connolly, M. L. The molecular surface package. *J. Mol. Graphics* **1993**, *11*, 139–141.

(19) Connolly, M. L. Analytical molecular surface calculation. *J. Appl. Crystallogr.* **1983**, *16*, 548–558.

(20) Connolly, M. L. Solvent-accessible surfaces of proteins and nucleic acids. *Science* **1983**, *221*, 709–713.

JP807706Q